remote sensing

MDPI

Article

Characterization and Removal of RFI Artifacts in Radar Data via Model-Constrained Deep Learning Approach

Mingliang Tao, **Jieshuang Li**, **Jia Su** and **Ling Wang** *

School of Electronics and Information, Northwestern Polytechnical University, Xi'an 710072, China; mltao@nwpu.edu.cn (M.T.); 2015301986@mail.nwpu.edu.cn (J.L.); jiasu1011@nwpu.edu.cn (J.S.)
* Correspondence: lingwang@nwpu.edu.cn

Abstract: Microwave remote sensing instruments such as synthetic aperture radar (SAR) play an important role in scientific research applications, while they suffer great measurement distortion with the presence of radio frequency interference (RFI). Existing methods either adopt model−based optimization or follow a data−driven black−box learning scheme, and both have specific limitations in terms of efficiency, accuracy, and interpretability. In this paper, we propose a hybrid model−constrained deep learning approach for RFI extraction and mitigation by fusing the classical model-based and advanced data-driven method. Considering the temporal-spatial correlation of target response, as well as the random sparsity property for time−varying interference, a joint low−rank and sparse optimization framework is established. Instead of applying the iterative optimization process with uncertain convergency, the proposed scheme approximates the iterative process with a stacked recurrent neural network. By adopting this hybrid model−constrained deep learning strategy, the original unsupervised decomposition problem is converted to a supervised learning problem. Experimental results show the validity of the proposed method under diverse RFI scenarios, which could avoid the manual tuning of model hyperparameters as well as speed up the efficiency.

Keywords: synthetic aperture radar; radio frequency interference; interference mitigation; model−constrained deep learning; hybrid framework

Citation: Tao, M.; Li, J.; Su, J.; Wang, L. Characterization and Removal of RFI Artifacts in Radar Data via Model-Constrained Deep Learning Approach. *Remote Sens.* **2022**, *14*, 1578. https://doi.org/10.3390/rs14071578

Academic Editor: Zhengxia Zou

Received: 17 January 2022
Accepted: 21 March 2022
Published: 24 March 2022

1. Introduction

1.1. Background and Motivation

Microwave remote sensing instruments like synthetic aperture radar (SAR) could operate day and night and serve as a versatile tool for a range of scientific applications in Earth observation. The spectrum use of earth exploration−satellite service (EESS) is strictly regulated by International Telecommunication Union (ITU) in certain frequency bands and inevitably shared with many other radio services, including radiolocation, space research, weather forecast [1], etc. The congested and contested spectrum usage makes the SAR system vulnerable to spurious radio signals, causing measure distortion, and these corrupting signals are referred to as radio frequency interference (RFI) [2].

1.2. Related Works

The RFI issues have drawn great attention in recent years due to adverse impact on accurate remote sensing, ranging from image formation process, image interpretation, as well as the accuracy of post−processing interferometric or polarimetric products [3,4]. Figure 1 compares particular examples acquired by the European Sentinel−1 system to illustrate the degradation to the imaging quality.

In recent years, a lot of effort has been devoted to alleviating the influence of residual RFI artifacts. A thorough review of existing mitigation techniques can be found in [5]. Generally, they can be categorized into model−based methods and data−driven methods based on their distinctive inference mechanism.

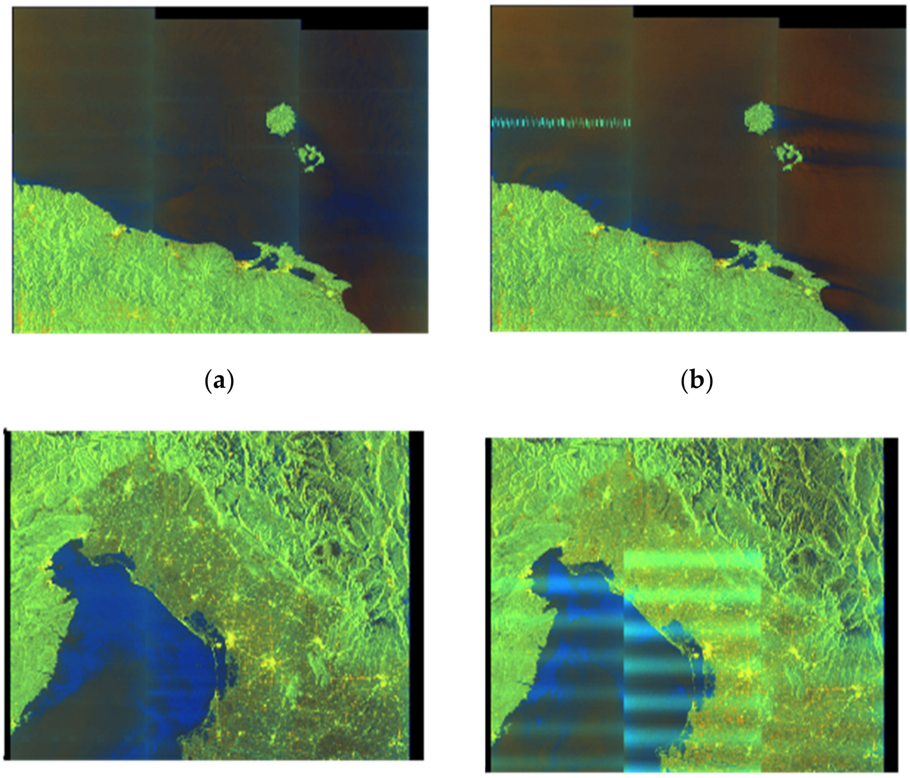

(**a**) (**b**)

(**c**) (**d**)

Figure 1. Comparison of SAR images with and without RFI artifacts acquired by the European Sentinel−1 system. The obvious artifacts in (**a**,**b**) are terrestrial interference, while in (**c**,**d**) they represent inter−satellite mutual interference.

The model−based approaches utilize mathematical expressions to represent the underlying physics and prior knowledge. One kind of advanced model−based mitigation technique utilizes the idea of signal decomposition, which manages to extract the latent components or subspaces corresponding to RFI according to property difference between RFI and target echoes, including the power, statistical difference, etc. Among them, the sparse and low−rank properties are well studied and demonstrated in [6–10] by employing the robust principal component analysis (RPCA) for a single scene in the raw data domain or image domain. Further, the idea is also extended to deal with time−series images in [11]. The RPCA approach can decompose the data matrix into a low−rank component and a sparse component via unsupervised iterative optimization. However, its efficiency is limited because of the relatively high dimension of the data matrix and uncertain convergence rate. Meanwhile, the model hyperparameters should be pre−defined empirically for the data according to prior knowledge. It is not a simple task in practical applications with diverse RFI scenarios and is also not suitable for mass processing in remote sensing applications [12].

On the other hand, with the advancement of deep learning approaches, data−driven intelligent learning methods have become an emerging trend for signal processing in recent years [13]. Thanks to the accumulation of big data in the remote sensing community, several neural network−based learning methods have shown superior performance and promising potential for efficient RFI detection and mitigation [14–18]. However, these methods are black−box in nature and lack certain interpretability. Their performance lies in the access of abundant data and immense computational resources, which limits the applicability for some practical scenarios with limited paired training samples.

1.3. Contributions

Figure 2 compares the pros and cons of these two types of approaches. Historically, the model−based method and the data−driven method have often been treated as two different fields with very different scientific paradigms [19]. However, these two schemes are complementary, with model−based approaches in principle being directly interpretable, whereas data−driven approaches are highly flexible in adapting to data and are amenable to discovering implicit features. To make full use of their respective merits and eliminate the deficiencies, we are investigating a hybrid fusing technique to explore the synergy between these two approaches, i.e., with the incorporation of principled domain knowledge and physical modelling into the design of data−driven network architecture [20,21].

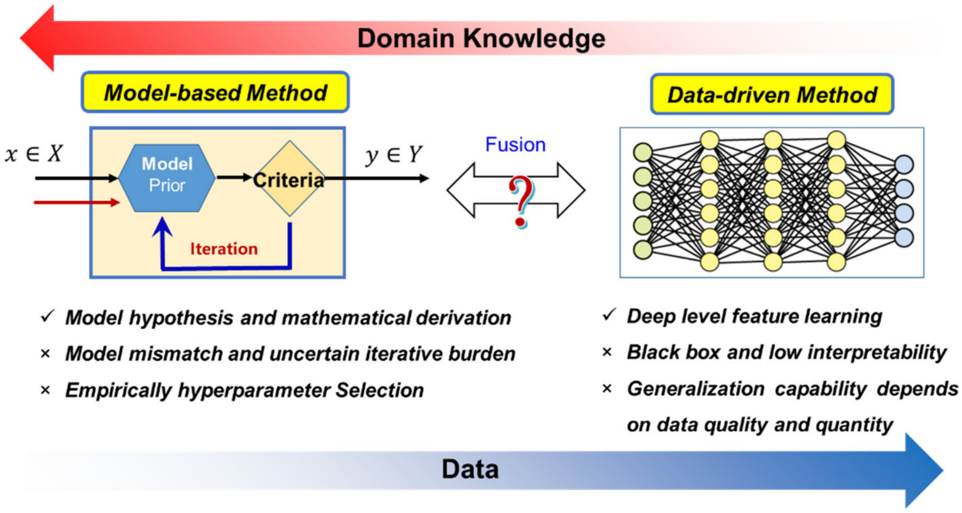

Figure 2. Hybrid fusion of model−based method and data−driven method.

In this paper, a model−constrained deep learning approach for RFI extraction and mitigation in SAR data is proposed. The main contributions are summarized as follows:

(1) This paper established a joint low−rank and sparse optimization framework by considering the temporalspatial correlation of target response, as well as the random sparsity property for time−varying interference. The model−based iterative optimization procedures are derived and propose an alternative recurrent neural networks (RNN) structure to imitate the iterative process, which improves the efficiency and provides an innovative insight into the traditional iterative optimization problems.

(2) In the proposed hybrid fusing scheme, the original unsupervised decomposition problem is equivalently converted to a supervised neural network−based learning problem. Unlike the generic off−the−shelf network structure, such a strategy incorporates partial domain knowledge via the underlying physical modeling into the network architecture. The model constrained network architecture is more interpretable, and the hyperparameters could be learned from reasonably sized training sets, rather than predefined through empirically manual tuning.

(3) The performance of the proposed method is verified on simulated and real measured experimental results under complicated heterogeneous scenarios with typical RFI types. It could achieve a better balance between efficiency and accuracy, which is beneficial for incorporation into the general automated processing flow of SAR data processing.

2. Problem Formulation

Figure 3 illustrates the interfering mechanism and the resulting received radar echoes. Under the stop−and−go model, for each azimuth time t_a, the discretized radar echoes

$x(n)$ could be modeled as a mixture of target echoes $s(n)$, interferences $i(n)$, and thermal noise $e(n)$ [22] without loss of generality, i.e.,

$$x(n) = s(n) + i(n) + e(n), \quad n = 1 \cdots N_r \tag{1}$$

where N_r denotes the samples along fast-time.

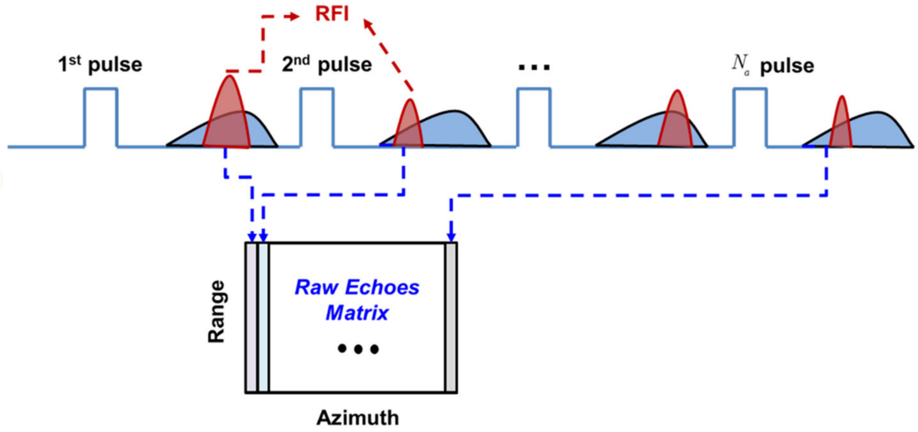

Figure 3. Illustration of the interfering mechanism and the resulting received radar echoes.

Generally, the goal of the RFI mitigation problem is to separate the interference and recover the echoes as much as possible. The solution to (1) is a single−channel signal source separation problem and is generally difficult to solve. Since RFI and target response are originated from different sources, the signal modulation characteristics are different. It is straightforward to characterize the RFI signatures in the time−frequency plane to maximize the non−overlapping portion of signals. The short time−frequency transform (STFT) is an efficient yet effective method, which can be represented as,

$$\mathbf{Y} = \sum_{m=0}^{M-1} h(m)x(n+m)e^{-j2\pi mk/M} \tag{2}$$

where $\mathbf{Y} \in \mathbb{C}^{P \times Q}$ is the resulting STFT complex spectrogram for the received echoes of a single pulse, and $h(m)$ is a sliding window with a length of M.

After performing the STFT transform on the adjacent N_a pulses' echoes, the complex spectrogram matrix of RFI-contaminated echoes $\mathbf{D} \in \mathbb{C}^{PQ \times N_a}$ is formed, as depicted in the left part of Figure 4. The rationale behind this consideration is the assumption that the adjacent echoes are highly correlated and possess low−rank properties. Moreover, the RFI is originated from uncorrelated sources and its pulse timing is not synchronous with the radar pules, which would present time−varying and sparse properties among different azimuth pulses, as shown in Figure 2. These assumptions are well demonstrated in previous studies [6–8].

Therefore, the RFI mitigation problem can be expressed as a general decomposition framework, i.e.,

$$\mathbf{D} = \mathbf{H}_1\mathbf{L} + \mathbf{H}_2\mathbf{S} + \mathbf{E} \tag{3}$$

where $\mathbf{L} \in \mathbb{C}^{PQ \times N_a}$ is assumed as a low-rank matrix corresponding to the target echoes attributes to its high temporal-spatial correlation. $\mathbf{S} \in \mathbb{C}^{PQ \times N_a}$ is assumed as a sparse matrix corresponding to the interference, since it appears randomly and sparsely on the 2-D data plane [7]. $\mathbf{H}_1$ and $\mathbf{H}_2$ are the measurement matrices of appropriate dimensions. $\mathbf{E}$ denotes the noise matrix. Figure 4 illustrates the physical model establishment process which incorporates the prior domain knowledge.

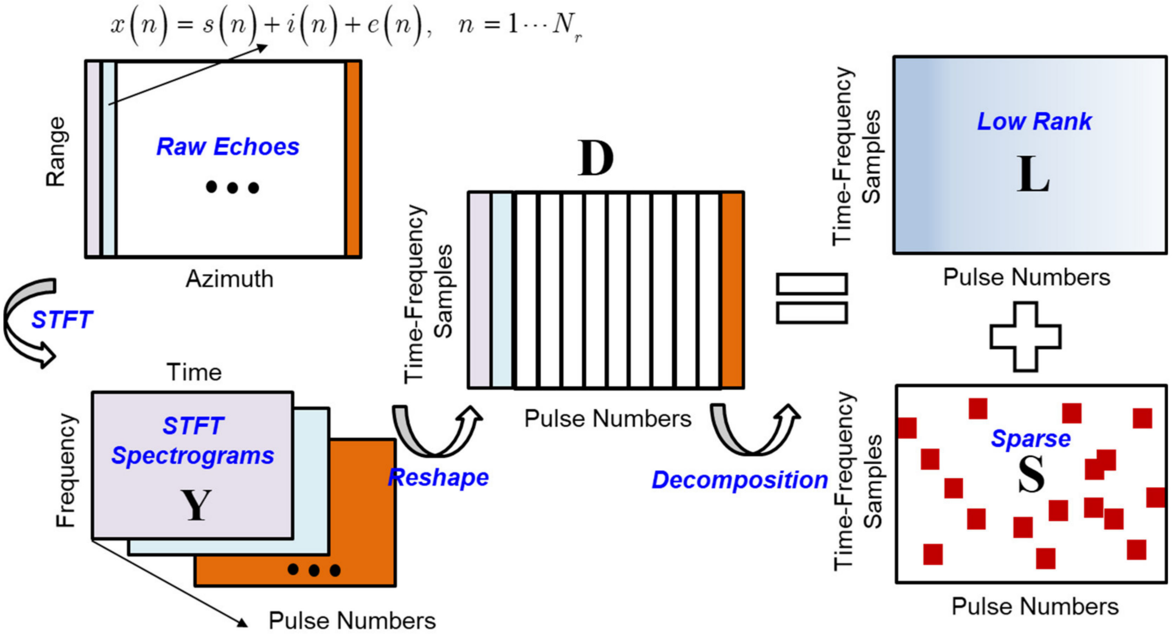

Figure 4. Representation of joint low−rank and sparse model for SAR data.

For RFI characterization and removal, the goal is managed to extract the latent components under the joint low−rank and sparse property assumption, which can be cast as a minimization problem,

$$\min_{\mathbf{L},\,\mathbf{S}} \frac{1}{2}\|\mathbf{D}-(\mathbf{H}_1\mathbf{L}+\mathbf{H}_2\mathbf{S})\|_F^2+\lambda_1\|\mathbf{L}\|_*+\lambda_2\|\mathbf{S}\|_{1,2} \tag{4}$$

where $\|\cdot\|_F$, $\|\cdot\|_*$ and $\|\cdot\|_{1,2}$ denotes the Frobenius norm, nuclear norm and the mixed $l_{1,2}$ norm, respectively. λ_1 and λ_2 are the regularized parameters that constrain the low-rank and sparsity property of the decomposition components.

Further, Equation (4) can be rewritten as

$$\min_{\mathbf{L},\,\mathbf{S}} \frac{1}{2}\|\mathbf{D}-\mathbf{A}\mathbf{X}\|_F^2+h(\mathbf{X}) \tag{5}$$

where $\mathbf{X}=[\mathbf{L};\mathbf{S}]$, $\mathbf{P}_1=[\mathbf{I};0]$, $\mathbf{P}_2=[0;\mathbf{I}]$, and $h(\mathbf{X})=\sum_{i=1}^{2}\lambda_i\rho_i(\mathbf{P_i}\mathbf{X})$, $\rho_1=\|\cdot\|_*$, $\rho_2=\|\cdot\|_{1,2}$.

The minimization problem is a regularized least−squares problem, which can be solved using the fast iterative shrinkage/thresholding algorithm (FISTA) [23], i.e.,

$$\mathbf{L}^{k+1}=SVT_{\lambda_1/L_f}\left\{\left(\mathbf{I}-\frac{1}{L_f}\mathbf{H}_1^H\mathbf{H}_1\right)\mathbf{L}^k-\mathbf{H}_1^H\mathbf{H}_2\mathbf{S}^k+\mathbf{H}_1^H\mathbf{D}\right\} \tag{6}$$

$$\mathbf{S}^{k+1}=T_{\lambda_2/L_f}\left\{\left(\mathbf{I}-\frac{1}{L_f}\mathbf{H}_2^H\mathbf{H}_2\right)\mathbf{S}^k-\mathbf{H}_2^H\mathbf{H}_1\mathbf{L}^k+\mathbf{H}_2^H\mathbf{D}\right\} \tag{7}$$

where $T_{\lambda_2/L_f}(\cdot)$ is the soft-thresholding operation, and $SVT_{\lambda_1/L_f}(\cdot)$ denotes the singular value thresholding operation. L_f is the Lipschitz constant of the quadratic term of (5).

By employing the iterative process shown in (6) and (7), the interference could be extracted out and eliminated. In this case, the measurement matrices $\mathbf{H}_1$ and $\mathbf{H}_2$ are identity matrices. Thus, the performance relies on the careful choice of hyperparameters λ_1 and λ_2, which is usually empirically set according to the specific dataset.

3. Theory and Methodology

In recent years, the proliferation of machine learning technologies has emerged in widespread disciplines to help generate new approaches derived from data. The universal approximation theorem states that any continuous function could be well approximated by a neural network with a single hidden layer containing a finite number of neurons [24]. Gregor et al. [25] prove the dramatic improvement in convergence by fusing the neural network into traditional model−based methods. Therefore, in this part, we will introduce a novel method to reformulate the iterative problem in (6) and (7).

The recurrent neural network is one of the state−of−the−art algorithms suited for problems involving sequential data. In an RNN unit, the information cycles through a loop to form an internal memory. That is, it considers the current input and the knowledge learned from previous inputs to make a decision. Figure 5 illustrates the structure of the recurrent neural network and its unrolled counterpart. The output and input relation between the RNN unit could be expressed as,

$$S_t = f(\mathbf{U}X_t + \mathbf{W}S_{t-1}) \tag{8}$$

$$Y_t = g(\mathbf{V}S_t + \mathbf{b}) \tag{9}$$

where S_t represent a hidden state at time instant t, and acts as the network memory. **U**, **V**, **W** and **b** are network hyperparameters that characterize the connection between input, hidden and output layers, and all these weights $(\mathbf{U}, \mathbf{V}, \mathbf{W}, \mathbf{b})$ are shared as fixed across time. $f(\cdot)$ and $g(\cdot)$ are nonlinear activation functions.

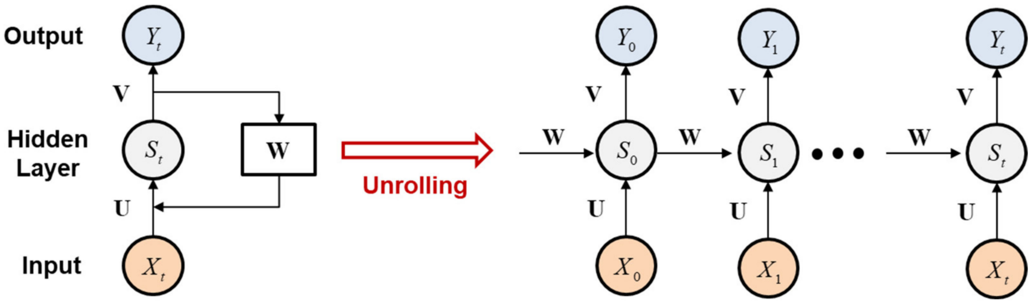

Figure 5. Notation of recurrent neural network and its unrolled counterpart.

As shown in Figure 5, the unrolling part is the equivalent expansion with the evolution of time. It is shown that the structure of RNN is very similar to the iterative process, in which the current output is related to the previous output in a recursive manner. Therefore, the algorithm unrolling provides a bridging connection between the iterative algorithms and the neural network [26]. Specifically, each iteration of the algorithm step could be represented as one layer of the network, and a deep neural network is formed by sequentially stacking these layers. In equivalence, when the information passes through the network it means that the iterative algorithm is executed a finite number of times.

Therefore, the problem becomes how to design appropriate architecture and determine parameterized matrices. By replacing the matrix multiplications in (6) and (7) with convolutional layers, the original iterative problem can be represented as [23],

$$\mathbf{L}^{k+1} = SVT_{\lambda_1^k}\left\{\mathbf{P}_5^k * \mathbf{L}^k + \mathbf{P}_3^k * \mathbf{S}^k + \mathbf{P}_1^k * \mathbf{D}\right\} \tag{10}$$

$$\mathbf{S}^{k+1} = T_{\lambda_2^k}\left\{\mathbf{P}_6^k * \mathbf{L}^k + \mathbf{P}_4^k * \mathbf{S}^k + \mathbf{P}_2^k * \mathbf{D}\right\} \tag{11}$$

where $*$ denotes the convolution operation. $\mathbf{P}_1^k, \cdots, \mathbf{P}_6^k$ denote the convolutional kernels of the $k-$th layer, in which the parameters are learned from the real−word training sets and may vary in each layer. Figure 6 illustrates the process of an equivalent replacement.

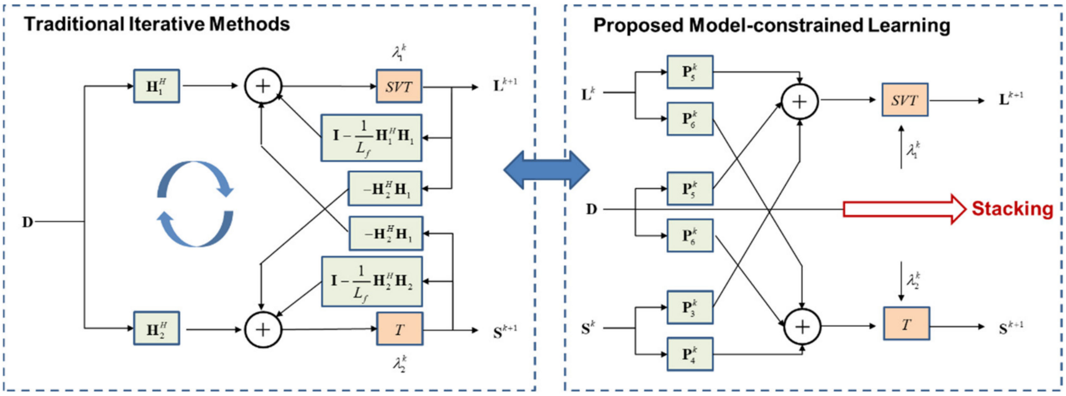

(**a**) (**b**)

Figure 6. The architecture of the proposed model−constrained deep learning approach. (**a**) Original iterative optimization problem. (**b**) Proposed equivalent replacement of stacked multi−layer RNN units.

The network is subsequently trained by the back−propagation method using paired inputs and outputs, and the loss function is chosen as the sum of the mean squared errors between the predicted values,

$$Loss(\vartheta) = \frac{1}{2N}\left(\sum_{i=1}^{N}\left\|f_S(\mathbf{D}_i,\vartheta)-\hat{\mathbf{S}}_i\right\|_F^2+\sum_{i=1}^{N}\left\|f_L(\mathbf{D}_i,\vartheta)-\hat{\mathbf{L}}_i\right\|_F^2\right) \tag{12}$$

where $\mathbf{D}_i$, $\hat{\mathbf{S}}_i$, $\hat{\mathbf{L}}_i$ are the training samples. N is the number of samples. $f_S(\mathbf{D}_i,\vartheta)$ and $f_L(\mathbf{D}_i,\vartheta)$ is the estimated sparse, low-rank components, respectively, which are determined by the parameter set $\vartheta = \left\{\mathbf{P}_1^k,\cdots,\mathbf{P}_6^k,\lambda_1^k,\lambda_2^k\right\}$.

By employing the transformation, the original unsupervised data−oriented iterative optimization problem is converted into a supervised learning problem. Compared with the original problem, it requires additional labeled ground−truth data for training. The unfixed iterative process is imitated by using the fixed multi−layer RNN units, which can speed up the iteration convergence. The regularization parameters are incorporated into the network and can be tuned automatically during the training process without manual determination. Compared with the generic data−driven methods, the proposed hybrid scheme inherits prior physical modelling knowledge to design the network architecture, which greatly improves the interpretability of the data−driven learning mechanism. Moreover, it entails fewer parameters and requires fewer training data. Therefore, the proposed hybrid fusion method adopts the merits of both kinds of approaches and tends to have better generalization performance.

4. Experimental Results and Discussions

4.1. Experimental Results of Synthetic Data

4.1.1. Experimental Setting

In this part, an airborne SAR dataset operates at X−band is used for the performance validation. Figure 7 summarizes the overall flowchart of the proposed processing scheme. Firstly, several representative RFI signals that are easily encountered in real scenarios, i.e., narrow−band interference, pulsed interference, wide−band interference, are simulated and randomly injected on the raw data echoes [27]. The number of echo samples for a single pulse is 4096, and it is transformed into spectrograms to form a stacked 3D data tensor of size 256 × 4096 × 20. Considering the relatively large dimension and to alleviate the computation burden of the training process, the entire 3−D tensor is divided into small sub−blocks of size 64 × 64, as shown in the left part of Figure 7. After forming the data tube and sub−blocks partition, the stacked RNN network undergoes the training process.

In this example, the number of RNN units are designed as 10 layers, in which the first three convolutional layers have a kernel size of 5 × 5 × 1, and the latter seven layers have a size of 3 × 3 × 1. In total, 2000 matrix samples were used for training, and 560 samples were used for testing. The Adam optimizer was employed to realize the learning process with a learning rate of 0.002. The initial value of the model hyperparameters λ_1, λ_2 are set arbitrarily as 0.4 and 1.8, respectively.

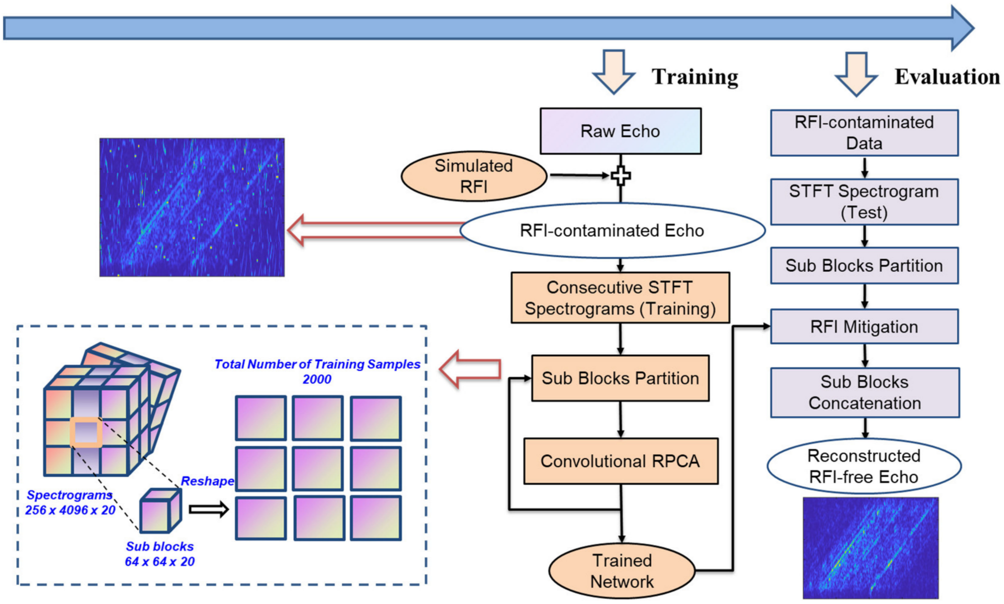

Figure 7. Overall workflow of the proposed scheme for RFI extraction and mitigation.

Figure 8 shows how the loss function changes with the iteration steps during the training phase. It shows that the training loss decreases gradually and fluctuates slightly after 50 epochs. After the training process, the well−trained network and its optimized hyperparameters are saved for further inference task. In the test phase, the data is also divided into small sub−blocks and undergoes a concatenation step after applying the proposed scheme.

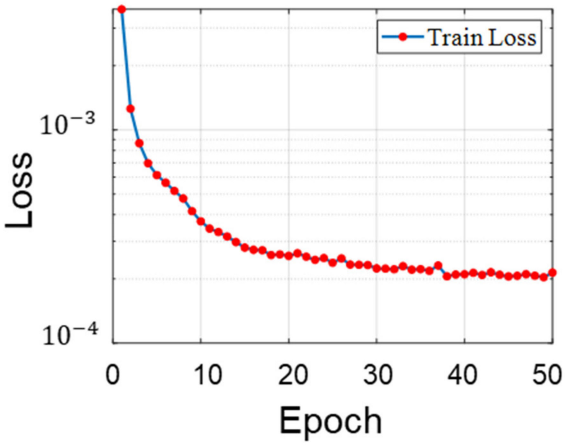

Figure 8. Variation of loss function value with iteration steps in the training phase.

4.1.2. Performance Discussion

For performance verification, two advanced decomposition methods including performance by PCA [22], RPCA [7], and BSF [28] were selected for comparison. The hyperparameters of both methods are optimally chosen after extensive comparison. Figures 9–11 show the interference estimation and mitigation results of two particular pulse echoes under four typical interference scenarios: narrowband interference, pulse interference, chirp modulated wideband interference, and sinusoidal modulated wideband interference. The essence of the proposed method is the time−frequency processing, and it has better performance when the interference is nonoverlapping and sparse compared with the target echo.

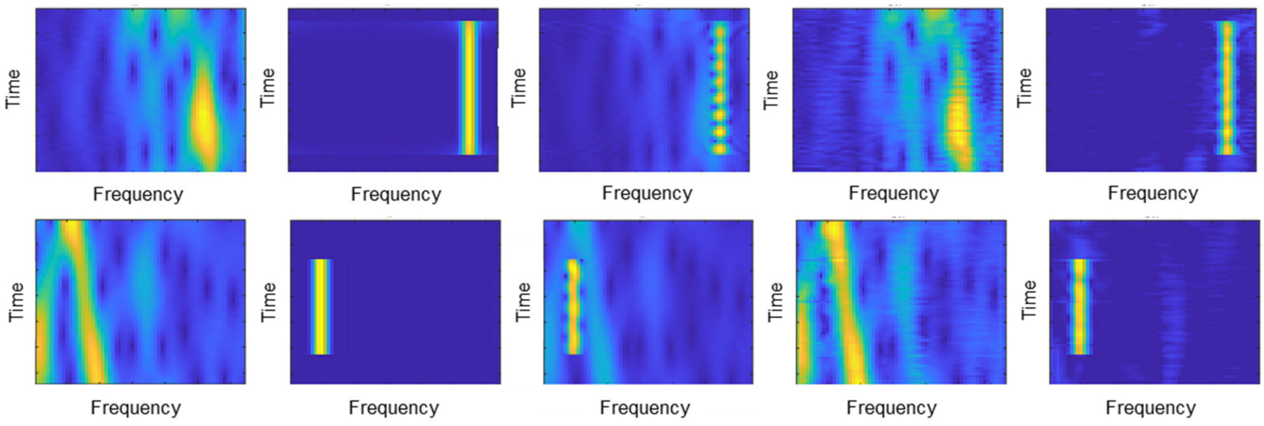

(**a**) (**b**) (**c**) (**d**) (**e**)

Figure 9. Comparison results of two particular sub−blocks for the narrowband RFI. (**a**) Original RFI−free spectrogram, (**b**) Simulated RFI, (**c**) RFI−contaminated spectrogram. (**d**) Estimated target response. (**e**) Extracted interference patterns. Each row corresponds to a particular pulse.

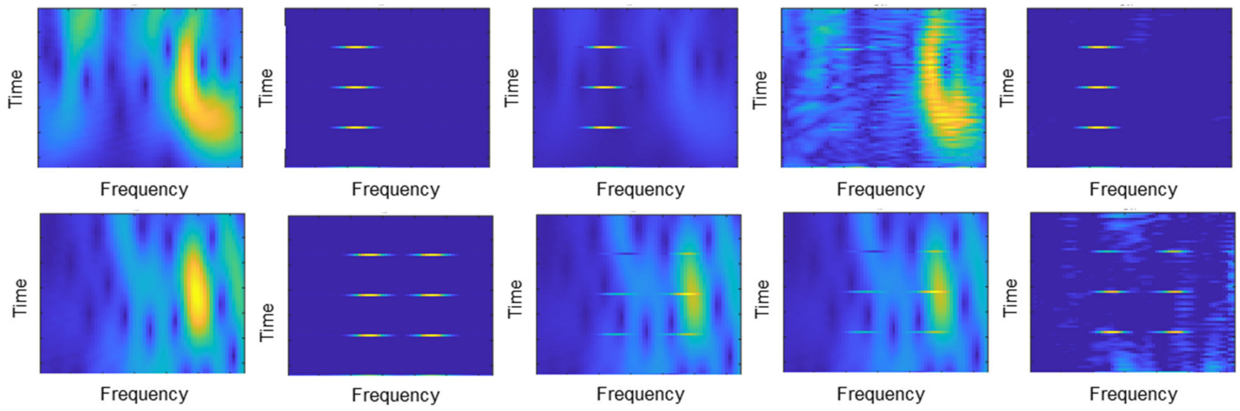

(**a**) (**b**) (**c**) (**d**) (**e**)

Figure 10. Comparison results of two particular sub−blocks for the pulsed RFI. (**a**) Original RFI−free spectrogram, (**b**) Simulated RFI, (**c**) RFI−contaminated spectrogram. (**d**) Estimated target response. (**e**) Extracted interference patterns. Each row corresponds to a particular pulse.

The previous part illustrates the results under different interference types. In the following, the robustness of the proposed method with strong and weak RFI energy is demonstrated. Figures 12 and 13 compare the interference extraction and mitigation performance of various methods under strong RFI and weak RFI, respectively. For the strong interference scenario, the targets echoes are covered up by the interference signatures and introduce large distortions, as shown in Figure 12a or Figure 13a. For the narrow−band interference case shown in Figure 12b–d, it is shown that the PCA and RPCA can recover the underlying spectrogram of the target echoes. As shown in the third column, the interference patterns estimated by the RPCA method are not continuous, indicating inaccurate characterization of the RFI artifacts. The proposed method shows superior performance for RFI elimination since the background residual is less and more approximate to the simulated RFI signatures.

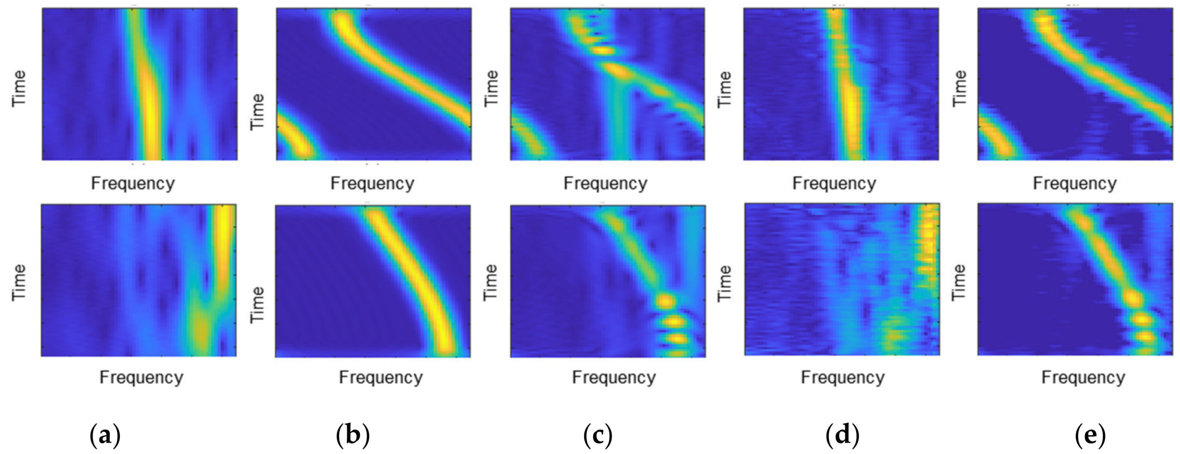

Figure 11. Comparison results of two particular sub−blocks for the chirp modulated RFI. (**a**) Original RFI−free spectrogram, (**b**) Simulated RFI, (**c**) RFI−contaminated spectrogram. (**d**) Estimated target response. (**e**) Extracted interference patterns. Each row corresponds to a particular pulse.

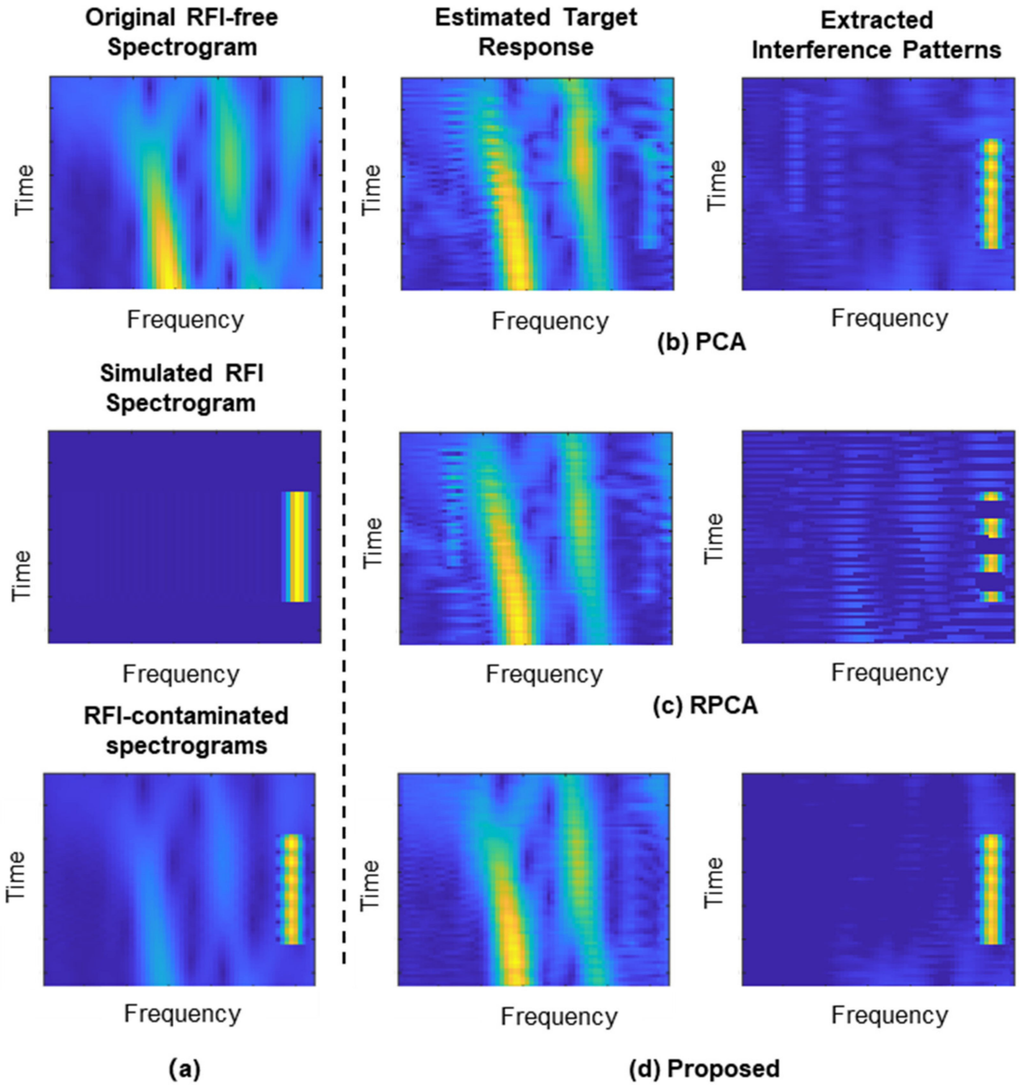

Figure 12. Comparison results for narrowband RFI with strong energy. (**a**) depicts the echoes for processing. (**b**–**d**) are the results of PCA, RPCA, and the proposed approach, respectively.

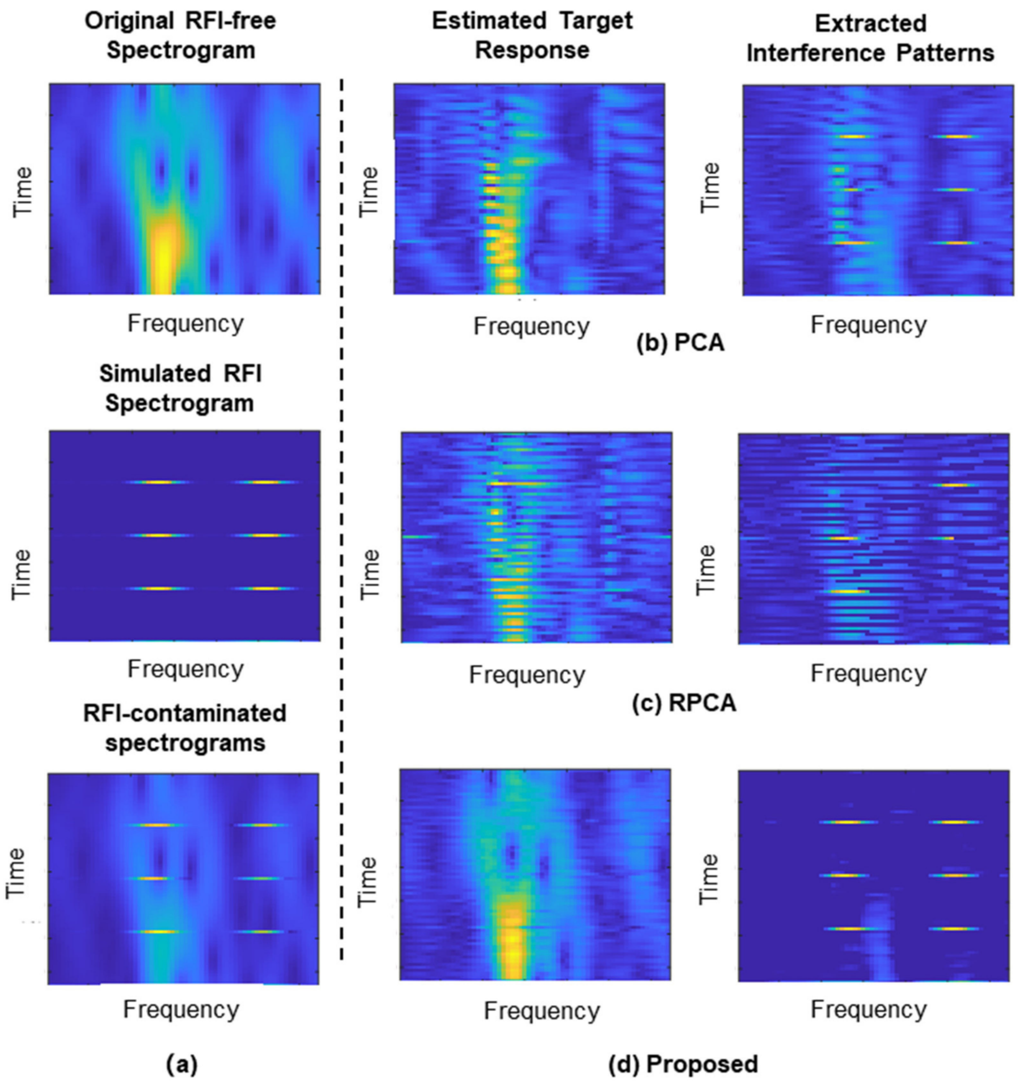

Figure 13. Comparison results for pulsed RFI with strong energy. (**a**) depicts the echoes for processing. (**b**–**d**) are the results of PCA, RPCA, and the proposed approach, respectively.

For the second case with pulsed interference, the PCA and RPCA present great performance degradation, in which the estimated target response and extracted RFI artifacts are still mixed, as shown in Figure 13b–d. In contrast, the proposed method can clearly estimate and extract RFI features from the data, effectively suppress the interference, and retain the effective information of the original data as much as possible.

Figures 14 and 15 compare the performance under weak RFI scenarios. As shown in Figure 14a or Figure 15a, the interference energy is much weaker than the original echo matrix. Compared with the original RFI−free spectrogram, the outline of the original information is still well captured even with RFI contamination. In this case, it increases the difficulty of RFI estimation and extraction.

As shown in Figure 14b–d or Figure 15b–d, the result of low−rank information recovery by RPCA is slightly better than that of PCA, whereas it is inferior to the proposed method. Moreover, in terms of the extracted RFI signatures, the PCA is better than the RPCA. For the RPCA, a single soft threshold would bias the result to one of the objectives of sparsity and low rank, resulting in more information loss of the RFI signatures. Since the interference energy is weak and the correlation between adjacent pulses is larger, the threshold in PCA is more biased towards the reconstruction of target echo. The proposed method is more accurate and robust, thanks to its hybrid fusion framework that both incorporates the domain knowledge, as well as learns the hyperparameters from the data. The proposed method has an adaptive soft threshold for each layer and enables better generalization capability for various RFI scenarios with diverse modulation types and energy.

Figure 16 shows the simulated echo data for performance comparison. Figure 17 compares the overall results after the concatenation of all the sub−blocks. It is shown that the RFI signatures are very complex, with raindrop−like artifacts overlapped with the target echoes in the whole time−frequency plane. The PCA and RPCA realize RFI extraction and mitigation with larger distortions to the target echoes. The proposed method extracts the RFI artifacts more clearly and the target echoes are preserved in good quality.

For quantitative comparison, the mean squared error (MSE) metric is used for performance evaluation, which is defined as

$$MSE = \frac{1}{K}\sum_{k=1}^{K}(\hat{y}_k - y_k)^2 \tag{13}$$

where $\hat{y}_k$ denotes the predicted values, and y_k denotes the original RFI-free samples, k is the number of samples.

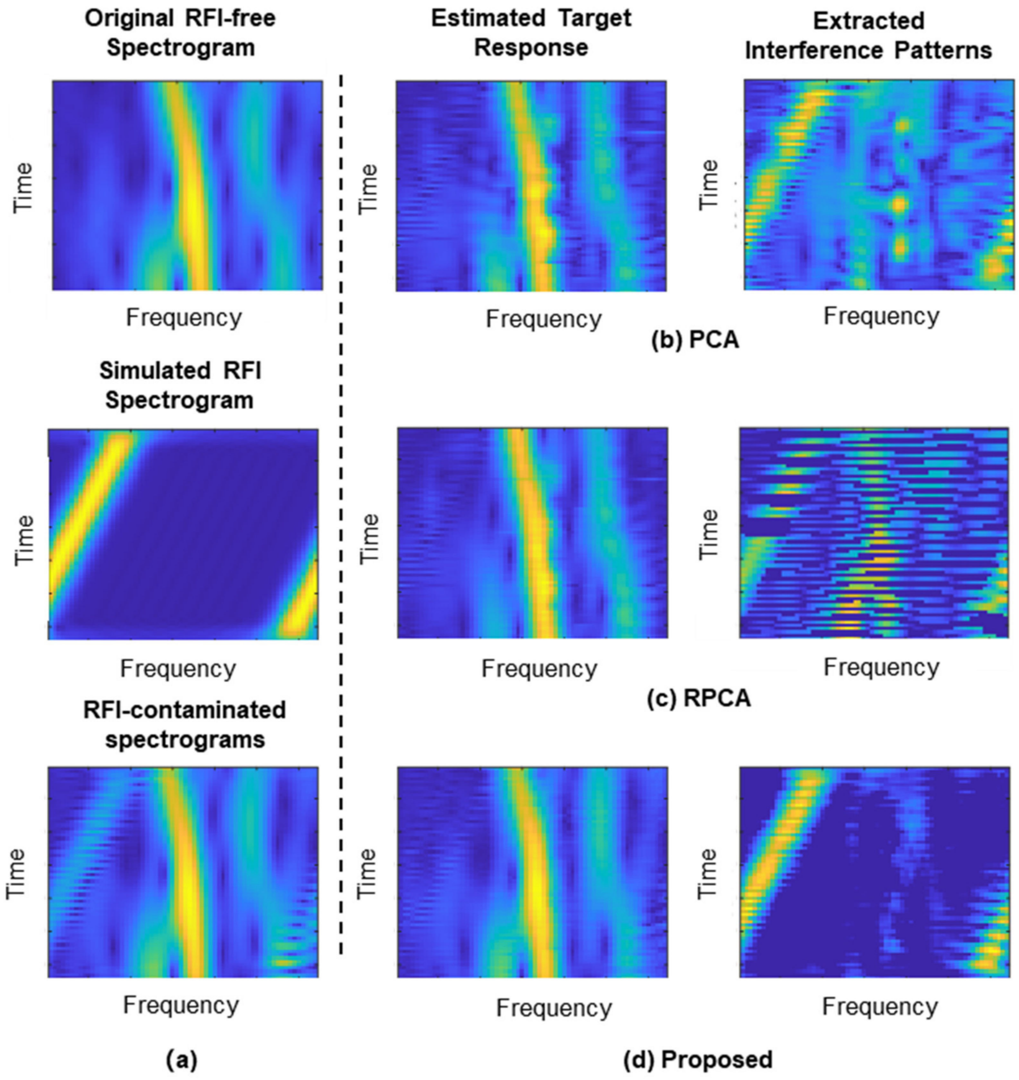

Figure 14. Comparison results for chirp modulated RFI with weak energy. (**a**) depicts the echoes for processing. (**b**–**d**) are the results of PCA, RPCA, and the proposed approach, respectively.

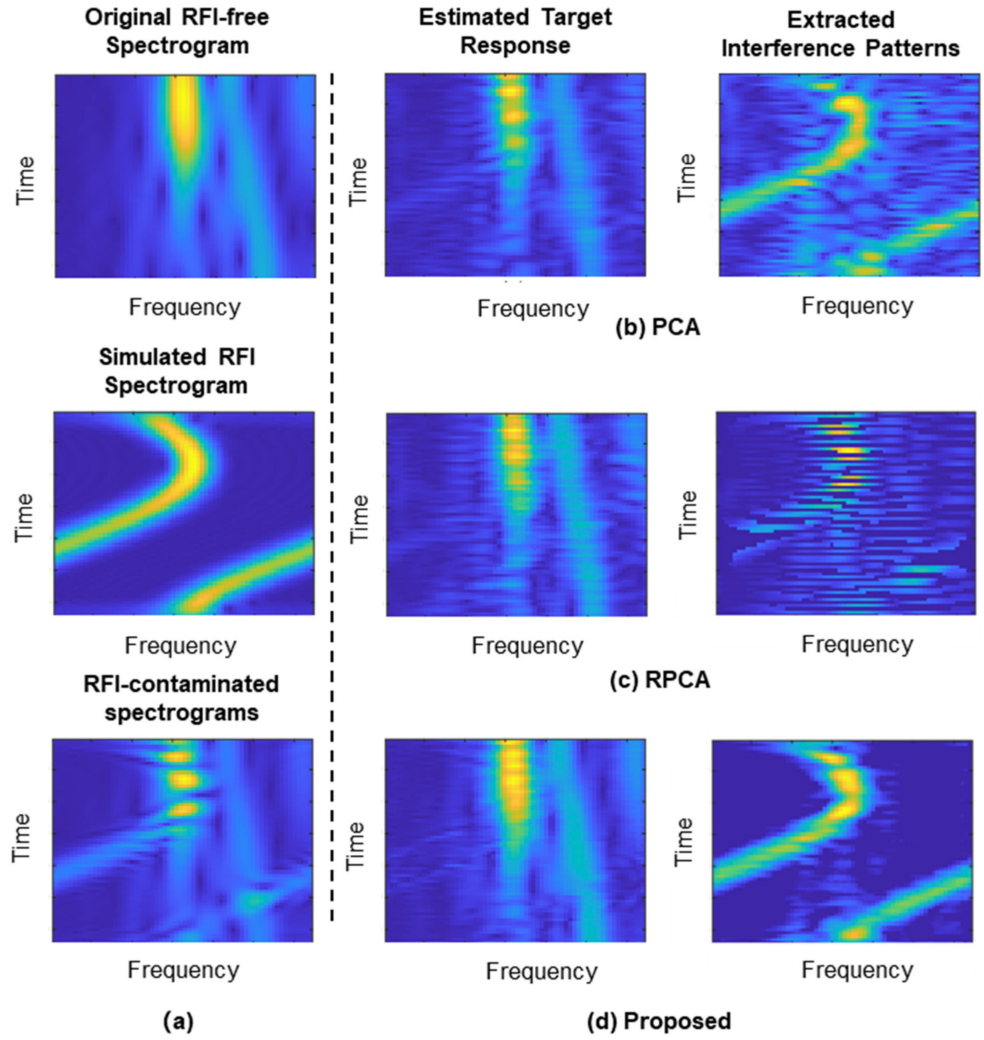

Figure 15. Comparison results for sinusoidal modulated RFI with weak energy. (**a**) depicts the echoes for processing. (**b**–**d**) are the results of PCA, RPCA, and the proposed approach, respectively.

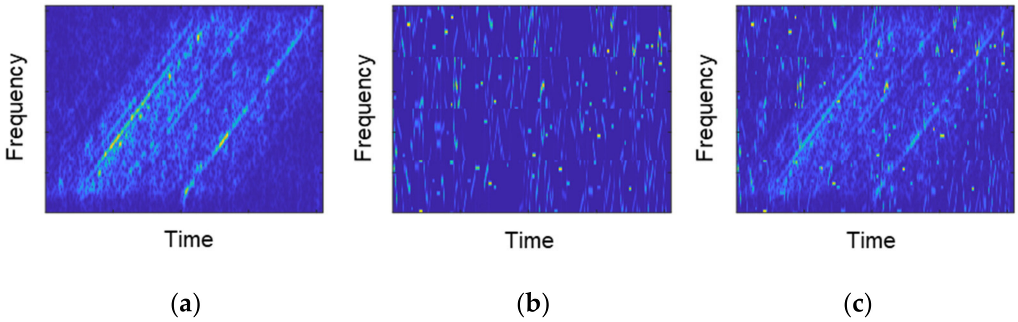

(**a**) (**b**) (**c**)

Figure 16. Simulated echoes for performance verification. (**a**) Original RFI−free spectrogram, (**b**) Simulated RFI, (**c**) RFI−contaminated spectrograms.

To verify the robustness of the proposed method, the performance under different signal to interference power ratio (SIR) is compared, as shown in Figure 18. From the curve, it indicates that the proposed method could achieve rather minimum reconstruction errors compared with other techniques, indicating a better characterization of the raw echo and less signal distortion.

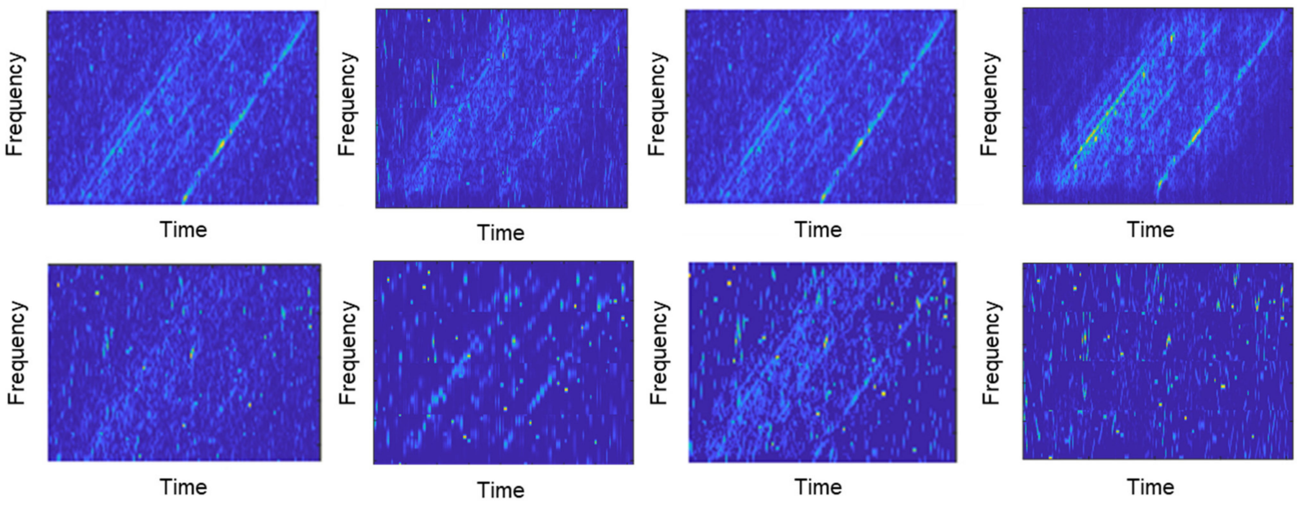

(**a**) (**b**) (**c**) (**d**)

Figure 17. Comparison results after applying (**a**) PCA, (**b**) BSF, (**c**) RPCA, and (**d**) the proposed approach.

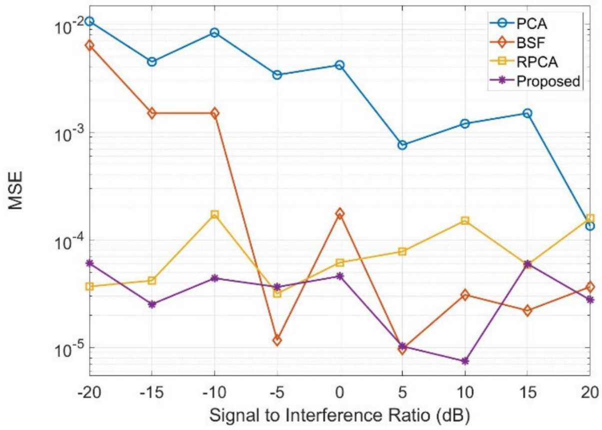

Figure 18. Variation of MSE with various signal to interference power ratios.

4.2. Experimental Results of Real—Measured Data

In this section, real—measured data is used for further demonstration. This data was acquired in the urban area of a city in western China. This dataset consists of various land covers, including the airport, civil buildings, and farm. The bandwidth of the transmitted signal is 180 MHz, and it is contaminated by spurious signals from the terrestrial radio services. Figure 19a shows the imaging results using the RFI-contaminated results. It is shown that the image is significantly distorted, due to the resulting strong RFI artifacts overlapping almost the whole scene. The overlapping artifacts cover up the target of interest such as the airport, making it rather difficult for the subsequent image interpretation applications. Figure 19b–d compare the RFI mitigation performance by PCA [22], RPCA [7], BSF [28], and proposed method, respectively. The hyperparameters of the baseline methods are well-tuned to achieve a best performance. Figure 20 shows the locally zoomed up results of the airport region. It is shown that after processing by PCA, the power of RFI artifacts tends to be alleviated, but still has significant residual foggy patterns spanning along the whole image plane. The BSF outperforms the PCA, in which the majority of the RFI artifacts are successfully mitigated. However, some residual bright lines still existed in the azimuth. The RPCA and the proposed method have a better performance from visual inspection, in which the airplanes on the airport and the land covers are clearly recovered.

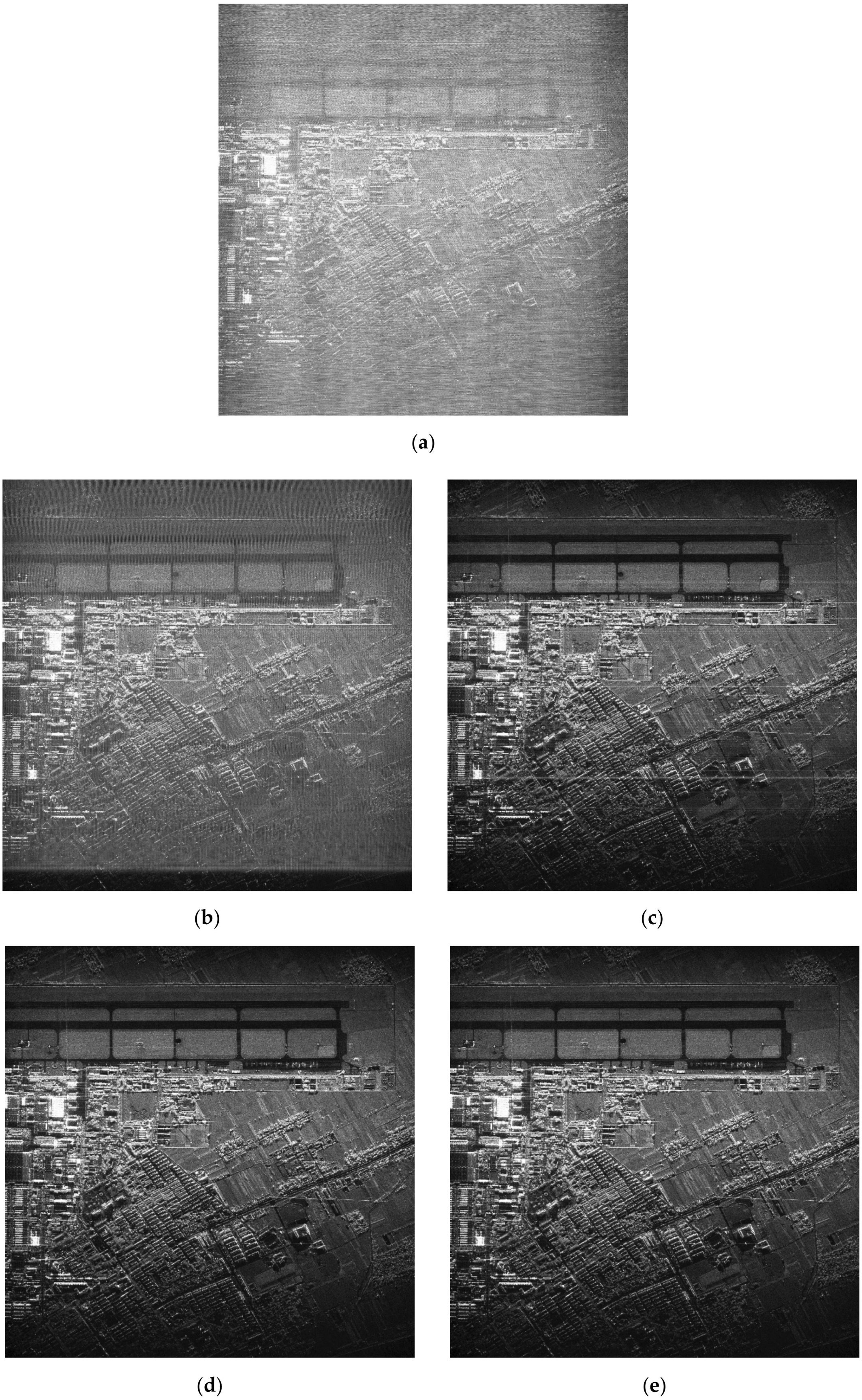

(**a**)

(**b**) (**c**)

(**d**) (**e**)

Figure 19. Comparison of imaging results. (**a**) RFI-contaminated image. (**b**) PCA, (**c**) BSF, (**d**) RPCA, and (**e**) proposed method.

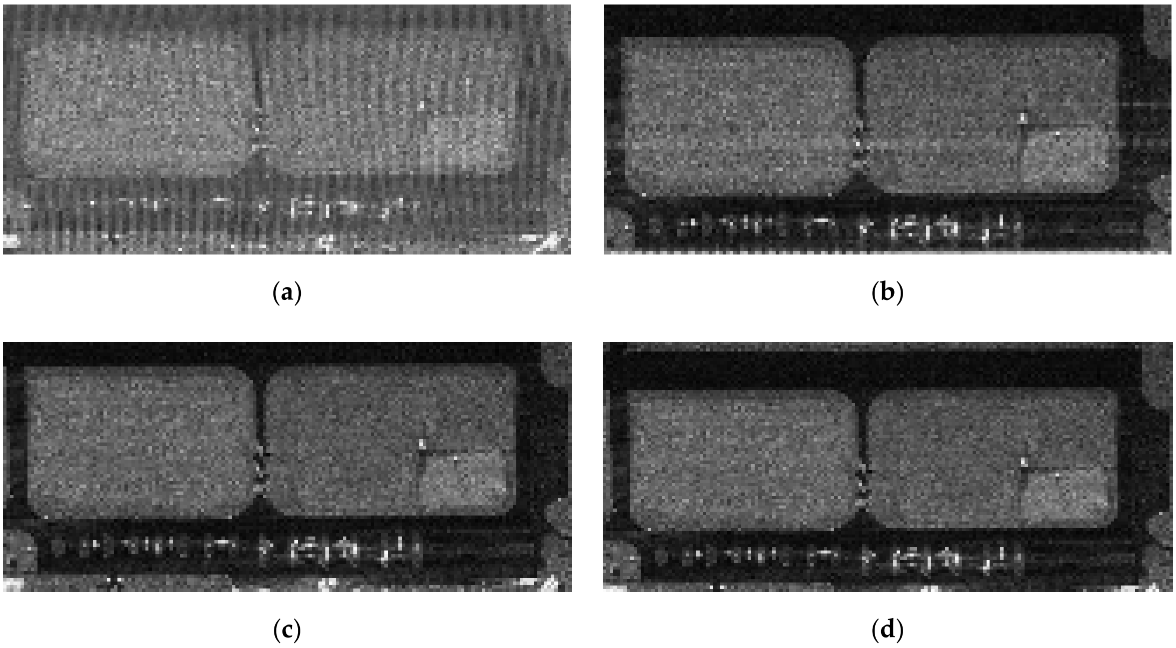
(**a**) (**b**) (**c**) (**d**)

Figure 20. Zoomed up results of the imaging results produced by (**a**) PCA, (**b**) BSF, (**c**) RPCA, and (**d**) proposed method.

To quantitatively evaluate the performance, we have selected two standard metrics to evaluate the image quality [29], i.e., the peak-signal-to-noise ratio (PSNR) and the structural similarity index measure (SSIM). The PSNR is an expression for the ratio between the maximum possible value (power) of a signal and the power of distorting noise that affects the quality. It represents a measure of the peak error and a higher PSNR indicates a better image quality. The SSIM is a perceptual metric that quantifies image quality degradation caused by processing and it is based on visible structures in the image. A larger value of SSIM represents a better mitigation performance. Table 1 lists the values of different methods, and it is shown that the proposed method could achieve a superior performance in terms of both metrics. These results are also consistent with previous qualitative evaluations.

Table 1. Imaging Evaluation Metrics for RFI Mitigation Performance.

Metrics	**PCA [22]**	**BSF [28]**	**RPCA [7]**	**Proposed**
PSNR	13.2132	18.7638	20.9084	22.2038
SSIM	0.1471	0.4734	0.5748	0.6780

5. Conclusions

RFI is a pervasive issue for the scientific applications of microwave remote sensing. Existing model-based or data-driven methods for RFI mitigation have made significant progress over the past few years, whereas it is difficult to achieve a balance between domain prior knowledge and data adaption. To alleviate this problem, this paper proposed a novel model-constrained deep learning scheme for RFI extraction and mitigation. The merits of the proposed method could be summarized as:

(1) From the data modeling perspective, the problem is formulated by principled physical modeling. Considering the spatial-temporal correlation between adjacent pulses, as well as the time-varying property of RFI, the problem is modelled as a joint low-rank and sparse decomposition issue. The original solution is achieved via unsupervised iterative optimization, in which the regularization parameters should be set as a priori and the convergence rate is not explicitly guaranteed.

(2) From the data characterization perspective, the proposed hybrid framework incorporates the recurrent neural network units to imitate the iterative process. By employing this replacement, the proposed hybrid framework can perform automatic tuning of hyperparameters, speed up the efficiency, and increase the interpretability of the network.

The proposed scheme provides new insight into the traditional iterative optimization problems and shows promising potential for solving complex problems. Besides the benefits, the proposed hybrid scheme has certain limitations in practical applications. Since the neural network techniques are data-dependent, the proposed method requires extra labeled data pairs for training compared with the original unsupervised decomposition problem. The conventional model-based method could be applied on a single data to realize RFI mitigation, while the proposed method should be well-trained beforehand with a cost of time for training. Moreover, the generalizability of the proposed method remains a common critical issue when performance on datasets are significantly different from those used during training. In the future, we would investigate a more refined fusing method for model-constrained deep learning and seek its application in radar signal processing.

Author Contributions: Conceptualization, M.T. and L.W.; methodology, M.T.; software, J.L.; validation, J.L.; writing—original draft preparation, M.T.; writing—review and editing, J.S. and L.W.; visualization, M.T. and J.S.; supervision, L.W. All authors have read and agreed to the published version of the manuscript.

Funding: This research was funded by National Nature Science Foundation of China (NSFC) under Grants 61801390 and 62171379. It was also partly funded by the Shanghai Aerospace Science and Technology Innovation Fund under grant SAST2021-044.

Institutional Review Board Statement: Not applicable.

Informed Consent Statement: Not applicable.

Data Availability Statement: Not applicable.

Acknowledgments: Thanks to the anonymous reviewers for valuable suggestions for improving the manuscript quality.

Conflicts of Interest: The authors declare no conflict of interest.

References

1. De Matthaeis, P.; Oliva, R.; Soldo, Y.; Cruz-Pol, S. Spectrum management and its importance for microwave remote sensing. *IEEE Geosci. Remote Sens. Mag.* **2018**, *6*, 17–25.
2. National Academies of Sciences Engineering and Medicine. *A Strategy for Active Remote Sensing Amid Increased Demand for Radio Spectrum*; National Academies Press: Washington, DC, USA, 2015.
3. Monti-Guarnieri, A.; Giudici, D.; Recchia, A. Identification of C-Band Radio Frequency Interferences from Sentinel-1 Data. *Remote Sens.* **2017**, *9*, 1183. [CrossRef]
4. Huang, Y.; Zhang, L.; Yang, X.; Chen, Z.; Liu, J.; Li, J.; Hong, W. An Efficient Graph-Based Algorithm for Time-Varying Narrowband Interference Suppression on SAR System. *IEEE Trans. Geosci. Remote Sens.* **2021**, *59*, 8418–8432. [CrossRef]
5. Tao, M.; Su, J.; Huang, Y.; Wang, L. Mitigation of Radio Frequency Interference in Synthetic Aperture Radar Data: Current Status and Future Trends. *Remote Sens.* **2019**, *11*, 2438. [CrossRef]
6. Huang, Y.; Zhang, L.; Li, J.; Chen, Z.; Yang, X. Reweighted Tensor Factorization Method for SAR Narrowband and Wideband Interference Mitigation Using Smoothing Multiview Tensor Model. *IEEE Trans. Geosci. Remote Sens.* **2020**, *58*, 3298–3313. [CrossRef]
7. Su, J.; Tao, H.; Tao, M.; Wang, L.; Xie, J. Narrow-Band Interference Suppression via RPCA-Based Signal Separation in Time–Frequency Domain. *IEEE J. Sel. Top. Appl. Earth Obs. Remote Sens.* **2017**, *10*, 5016–5025. [CrossRef]
8. Joy, S.; Nguyen, L.H.; Tran, T.D. Joint Down-Range and Cross-Range RFI Suppression in Ultra-Wideband SAR. *IEEE Trans. Geosci. Remote Sens.* **2020**, *99*, 3136–3149. [CrossRef]
9. Lu, X.; Yang, J.; Yeo, T.S.; Su, W.; Gu, H.; Yu, W. Accurate SAR Image Recovery from RFI Contaminated Raw Data by Using Image Domain Mixed Regularizations. *IEEE Trans. Geosci. Remote Sens.* **2021**, *60*, 5102813. [CrossRef]
10. Yang, H.; Chen, C.; Chen, S.; Xi, F.; Liu, Z. SAR RFI Suppression for Extended Scene Using Interferometric Data via Joint Low-Rank and Sparse Optimization. *IEEE Geosci. Remote Sens. Lett.* **2020**, *18*, 1976–1980. [CrossRef]
11. Tao, M.; Lai, S.; Li, J.; Su, J.; Fan, Y.; Wang, L. Extraction and Mitigation of Radio Frequency Interference Artifacts Based on Time-Series Sentinel-1 SAR Data. *IEEE Trans. Geosci. Remote Sens.* **2021**, *60*, 5217211. [CrossRef]

12. Santamaria, C.; Alvarez, M.; Greidanus, H.; Syrris, V.; Soille, P.; Argentieri, P. Mass Processing of Sentinel-1 Images for Maritime Surveillance. *Remote Sens.* **2017**, *9*, 678. [CrossRef]
13. Itschner, I.; Li, X. Radio frequency interference (RFI) detection in instrumentation radar systems: A deep learning approach. In Proceedings of the 2019 IEEE Radar Conference (RadarConf), Boston, MA, USA, 22–26 April 2019.
14. Artiemjew, P.; Chojka, A.; Rapiński, J. Deep Learning for RFI Artifact Recognition in Sentinel-1 Data. *Remote Sens.* **2021**, *13*, 7. [CrossRef]
15. Fan, W.; Zhou, F.; Tao, M.; Bai, X.; Rong, P.; Yang, S.; Tian, T. Interference Mitigation for Synthetic Aperture Radar Based on Deep Residual Network. *Remote Sens.* **2019**, *11*, 1654. [CrossRef]
16. Tao, M.; Tang, S.; Li, J.; Zhang, X.; Fan, Y.; Su, J. Radio Frequency Interference Detection for SAR Data Using Spectro-gram-Based Semantic Network. In Proceedings of the 2021 IEEE International Geoscience and Remote Sensing Symposium IGARSS, Brussels, Belgium, 11–16 July 2021; pp. 1662–1665.
17. Yu, J.; Li, J.; Sun, B.; Chen, J.; Li, C. Multiclass Radio Frequency Interference Detection and Suppression for SAR Based on the Single Shot MultiBox Detector. *Sensors* **2018**, *18*, 4034. [CrossRef]
18. Yan, R.-Q.; Dai, C.; Liu, W.; Li, J.-X.; Chen, S.-Y.; Yu, X.-C.; Zuo, S.-F.; Chen, X.-L. Radio frequency interference detection based on the AC-UNet model. *Res. Astron. Astrophys.* **2021**, *21*, 119. [CrossRef]
19. Reichstein, M.; Camps-Valls, G.; Stevens, B.; Jung, M.; Denzler, J.; Carvalhais, N. Deep learning and process under-standing for data-driven Earth system science. *Nature* **2019**, *566*, 195–204.
20. Shlezinger, N.; Whang, J.; Eldar, Y.C.; Dimakis, A.G. Model-Based Deep Learning. *arXiv* **2020**, arXiv:2012.08405.
21. Tao, M.; Li, J.; Su, J.; Fan, Y.; Wang, L. Extraction and Analysis of RFI Signatures via Deep Convolutional RPCA. In Proceedings of the 2021 XXXIVth General Assembly and Scientific Symposium of the International Union of Radio Science (URSI GASS), Rome, Italy, 28 August–4 September 2021. [CrossRef]
22. Yang, H.; Tao, M.; Chen, S.; Xi, F.; Liu, Z. On the mutual interference between spaceborne SARs: Modeling, characterization, and mitigation. *IEEE Trans. Geosci. Remote Sens.* **2020**, *59*, 8470–8485.
23. Solomon, O.; Cohen, R.; Zhang, Y.; Yang, Y.; He, Q.; Luo, J.; van Sloun, R.J.G.; Eldar, Y.C. Deep Unfolded Robust PCA with Application to Clutter Suppression in Ultrasound. *IEEE Trans. Med. Imaging* **2020**, *39*, 1051–1063. [CrossRef]
24. Lu, Y.; Lu, J. A universal approximation theorem of deep neural networks for expressing probability distributions. *arXiv* **2020**, arXiv:2004.08867.
25. Gregor, K.; LeCun, Y. Learning fast approximations of sparse coding. In Proceedings of the 27th International Conference on International Conference on Machine Learning, Haifa, Israel, 21–24 June 2010; pp. 399–406.
26. Monga, V.; Li, Y.; Eldar, Y.C. Algorithm unrolling: Interpretable, efficient deep learning for signal and image processing. *IEEE Signal Processing Mag.* **2021**, *38*, 18–44.
27. Querol, J.; Onrubia, R.; Alonso-Arroyo, A.; Pascual, D.; Park, H.; Camps, A. Performance Assessment of Time-Frequency RFI Mitigation Techniques in Microwave Radiometry. *IEEE J. Sel. Top. Appl. Earth Obs. Remote Sens.* **2017**, *10*, 3096–3106. [CrossRef]
28. Yang, H.; Li, K.; Li, J.; Du, Y.; Yang, J. BSF: Block Subspace Filter for Removing Narrowband and Wideband Radio Interference Artifacts in Single-Look Complex SAR Images. *IEEE Trans. Geosci. Remote Sens.* **2022**, *60*, 5211916.
29. Hore, A.; Ziou, D. Image quality metrics: PSNR vs. SSIM. In Proceedings of the 2010 20th International Conference on Pattern Recognition, Istanbul, Turkey, 23–26 August 2010; pp. 2366–2369.